Spin-flop transition in the quasi-two-dimensional antiferromagnet MnPS3 detected via thermally generated magnon transport

Feringa, F.; Vink, J. M.; Van Wees, B. J.

Published in:
Physical Review B

DOI:
10.1103/PhysRevB.106.224409

Publication date:
2022

Spin-flop transition in the quasi-two-dimensional antiferromagnet $MnPS_3$ detected via thermally generated magnon transport

F. Feringa,* J. M. Vink, and B. J. van Wees†
Physics of Nanodevices, Zernike Institute for Advanced Materials, University of Groningen, 9747 AG Groningen, Netherlands

(Received 2 September 2022; revised 15 November 2022; accepted 16 November 2022; published 12 December 2022)

We present the detection of the spin-flop transition in the antiferromagnetic van der Waals material $MnPS_3$ via thermally generated nonlocal magnon transport using permalloy (Py) detector strips. Py detector strips possess the inverse anomalous spin Hall effect, which has the unique power to detect an out-of-plane spin accumulation [Das *et al.*, Nano Lett. **18**, 5633 (2018)]. This enables us to detect magnons with an out-of-plane spin polarization, in contrast to strips of high-spin-orbit materials such as Pt which possess only the spin Hall effect and are sensitive to only an in-plane spin polarization of the spin accumulation. We show that nonlocal magnon transport is able to measure the spin-flop transition in the absence of spurious magnetoresistance effects. Our measurements show the detection of magnons generated by the spin Seebeck effect before and after the spin-flop transition. We observe a signal reversal of the magnon spin accumulation which agrees with the out-of-plane spin polarization carried by magnon modes before and after the spin-flop transition.

DOI: 10.1103/PhysRevB.106.224409

I. INTRODUCTION

The recent discovery of long-range magnetic ordering in two-dimensional magnets [1,2] opens possibilities to study and explore the magnetic structure and dynamics in two-dimensional magnets [3]. Especially, antiferromagnetic materials have attracted great interest for information storage and as a medium for spin currents in spintronic devices because they do not possess stray fields, are robust against magnetic perturbations, and have ultrafast magnetic dynamics [4,5]. Antiferromagnets possess a variety of spin textures, for example, uniaxial, easy-plane, and noncolinear spin textures, determined by the material-specific values of the exchange field and anisotropy field parameters. Additionally, magnetic van der Waals materials often have much stronger intralayer exchange interactions than interlayer exchange interactions, giving magnetic van der Waals materials a rich variety of spin textures.

Characterizing and probing magnetic transitions in (quasi-) two-dimensional magnetic van der Waals materials are crucial to understand magnetism at a low-dimensional limit, for example, by characterizing the spin-flop (SF) transition in uniaxial antiferromagnets (AFMs). When the applied magnetic field H_0 exceeds the spin-flop field H_{SF} at the SF transition, the spin configuration changes from (anti)parallel to (almost) perpendicular to the magnetic field. The SF transition has been studied using magnetic measurements [6]. This is difficult for thin (low-volume) magnetic layers; however, as an alternative magnons can be used to study the SF transition electrically. At the spin-flop field, the energy for certain magnon modes goes to zero, which should result in a strong modification and even sign reversal of the spin polarization of the magnon generated by the spin Seebeck effect.

Magnon spintronics uses magnons to transport angular momentum, which is a unique tool to investigate magnetic dynamics in magnetic materials because it can characterize magnetic van der Waals materials down to a monolayer using a heterostructure of a heavy (ferromagnetic) metal and the magnetic layer. Magnon transport has been extensively studied in three-dimensional (3D) magnets via spin pumping [7–10], the spin Seebeck effect [11–13], and electrical injection and detection [14,15]. Nonlocal magnon transport has been observed in ferrimagnets [14,16] and antiferromagnets [1,17–20]. It has been shown that the SF transition in Cr_2O_3 (3D), for which the spins lie in plane before and after the SF transition, can be probed locally via the spin Seebeck effect using Pt [21,22] and permalloy (Py) [23] contacts. The spin Hall magnetoresistance detected the SF transition in Pt or Pd in contact with the van der Waals AFM $CrPS_4$. This was detected locally, and therefore, spin Hall magnetoresistance (SMR) probes only the magnetic properties in the first layer(s) of the AFM in contact with the heavy metal [24]. Detecting the SF transition via thermally generated magnons in a nonlocal geometry in van der Waals magnets has not been investigated. This has the benefit of studying the SF transition in a magnetic material outside the proximity of a heavy metal. Moreover, as we will show, no spurious (thermal) effects are present in the detector strips except for an anomalous Nernst effect which can be subtracted in a straightforward way.

In this work, we detect the SF transition in the antiferromagnetic transition metal trichalcogenide $MnPS_3$ using thermally generated magnons which we detect nonlocally using Pt and Py contacts. A heater generates a temperature gradient in $MnPS_3$ which generates magnons via the spin Seebeck effect which are detected at a Pt or Py detector. This is a very clean way of measuring due to the lack of other spurious

*F.Feringa@rug.nl
†B.J.van.Wees@rug.nl

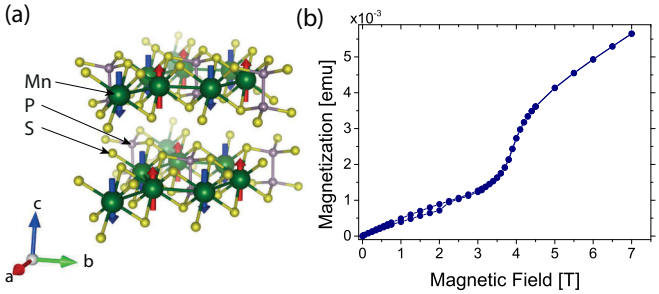

FIG. 1. (a) Spin structure of $MnPS_3$. The red and blue arrows denote the spin direction in the absence of a magnetic field. (b) Magnetization measured for an applied out-of-plane magnetic field. The spin-flop transition is observed around 3.7 T, indicated by the sharp increase of the magnetization.

effects in the detector strips and in the absence of a temperature gradient across the interface of the detector strips (see Appendix B). The magnetic easy axis in $MnPS_3$ is out of plane (OOP), i.e., perpendicular to the a-b plane, and therefore, the generated magnons carry spins with an OOP polarization. These spins cannot be detected via the regular inverse spin Hall effect (ISHE), which generates only a charge current for a spin current with an in-plane spin polarization. However, the inverse anomalous Hall effect (IASHE) is able to detect a spin current with an OOP spin polarization, for example, using Py contacts [25,26]. We show that the Py contacts can detect the spin-flop transition in $MnPS_3$ via magnons which carry spins with an OOP spin polarization via the IASHE in Py. We find that the polarization of the spins carried by the magnon changes sign when crossing the SF transition and that the detected signal is maximum when the energy of the relevant magnon modes go to zero.

Antiferromagnets are characterized by two order parameters, the Néel vector $\vec{n} = \vec{m}_1 - \vec{m}_2$ and the net magnetization $\vec{m} = \vec{m}_1 + \vec{m}_2$. An easy-axis antiferromagnet undergoes a SF transition when the applied magnetic field strength along the easy axis exceeds the spin-flop field $H_{\mathrm{SF}} = \sqrt{2H_{\mathrm{A}}H_{\mathrm{E}} - H_{\mathrm{A}}^2}$, where H_{A} is the anisotropy field and H_{E} is the exchange field strength of the antiferromagnetic material. After the spin-flop transition, the spins cant towards the applied magnetic field direction.

Dynamically, antiferromagnets possess a variety of magnon modes depending on the state of the antiferromagnet, as presented in Figs. 2(a)–2(c). Below the SF transition, the degeneracy of the two magnon modes is lifted by the Zeeman splitting when a magnetic field is applied, and therefore, one magnon mode, ω_β, decreases, and magnon mode ω_α increases in energy, as shown in Fig. 2(d) for the $k = 0$ magnon modes. When exciting the magnon modes at a finite temperature, the lower-energy mode, ω_β, whose which spin is oriented *along* the magnetic field direction, is populated more. Above the SF, the magnon modes ω_β carry spins with a polarization in the z direction *opposite* to the magnetization order parameter $\vec{m}$, and therefore, the spin polarization in the z direction of the magnons is *opposite* to the applied magnetic field direction. Consequently, the spin polarization direction of the magnons changes from parallel to antiparallel to the applied magnetic field direction crossing the SF transition.

In a magnetic insulator a magnon spin current can be generated due to a temperature gradient in a magnetic material via the spin Seebeck effect (SSE), which can be expressed as [27]

$$J_S^z = S_S^z \nabla T. \tag{1}$$

At zero magnetic field the magnon modes I′ are degenerate, and therefore, under the influence of a temperature gradient both modes are populated equally. The modes carry opposite angular momenta, and therefore, no net spin current is present. An imbalance in population between the modes is present at a finite magnetic field, resulting in a finite net spin current. The spin Seebeck coefficient S_S^z depends on the difference in occupation of the different magnon modes [28]. At the SF transition, mode ω_β reaches zero, and therefore, the largest S_S^z is expected.

The total detected voltage is given by [29]

$$V_{\mathrm{NL}} = GS_S^z, \tag{2}$$

where $G \propto R_N w \lambda_N \frac{2e}{\hbar} \theta_{\mathrm{ASH}} \tanh(\frac{t_N}{2\lambda_N}) C g^{\uparrow\downarrow} \vec{\nabla} T$, with R_N being the resistance, t_N being the thickness, w being the width, θ_{ASH} being the anomalous spin Hall angle, and λ_N being the spin relaxation length of the detector strip. $g^{\uparrow\downarrow}$ is the effective spin mixing conductance, and C contains the thickness, magnon diffusion length, geometry of the nonlocal device, and other material parameters.

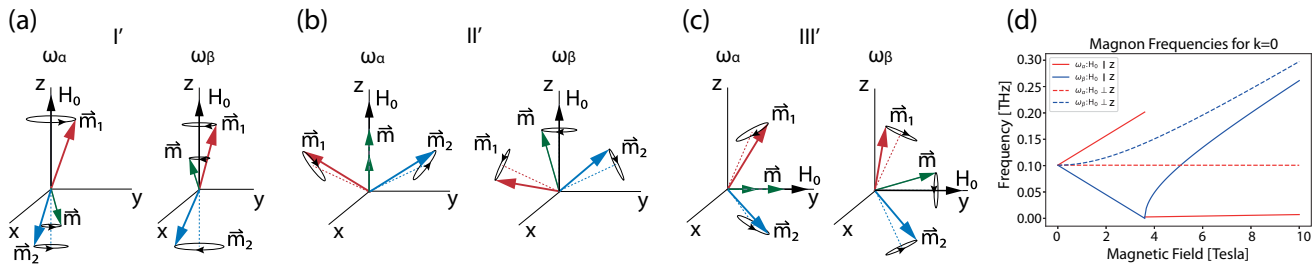

FIG. 2. (a)–(c) Magnon modes I′, II′, and III′. (a) I′ possesses two circular polarized magnon modes ω_α and ω_β. (b) After the spin-flop transition, II′ possesses a magnon mode ω_α linearly polarized in $\vec{n}$ and $\vec{m}$ and a magnon mode ω_β which is linearly polarized in $\vec{n}$ and circular polarized in $\vec{m}$. (c) III′ possesses magnon modes similar to those of II′, but the order parameters $\vec{n}$ and $\vec{m}$ point in a different direction. (d) $k = 0$ frequencies for magnon modes I′, II′, and III′ are plotted.

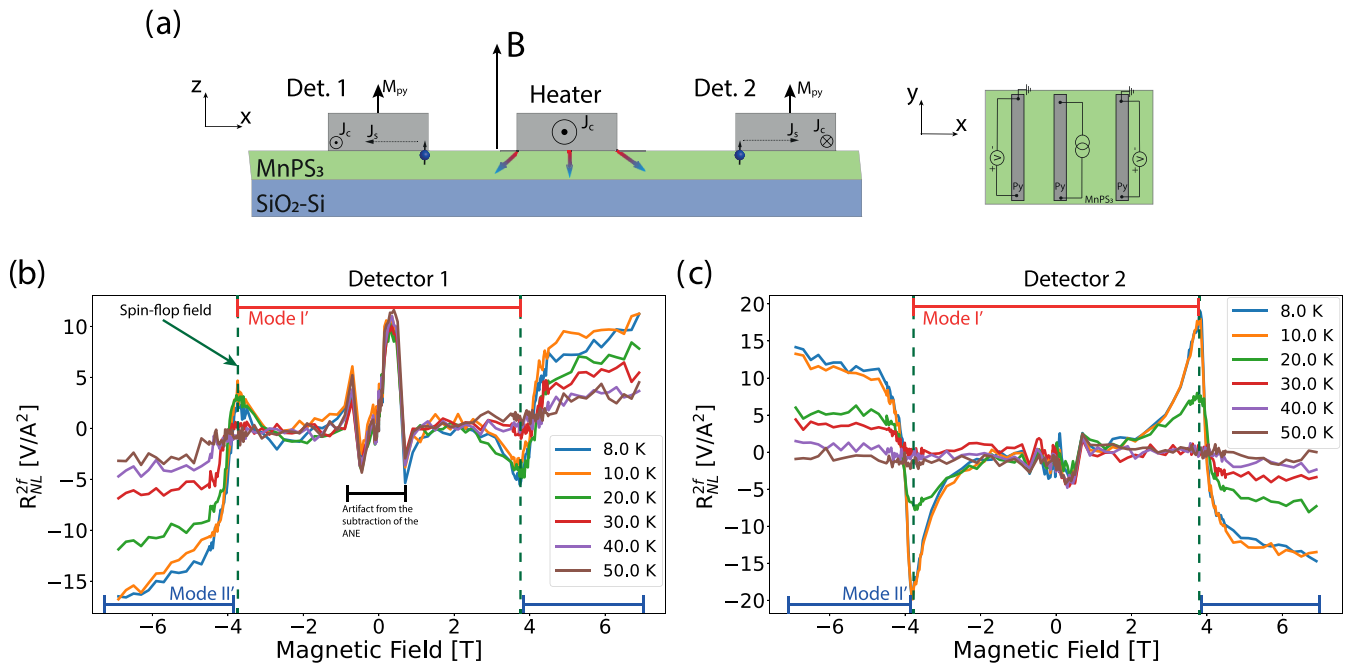

FIG. 3. (a) Illustration of the device geometry. A Py heater and detector strips on $MnPS_3$ are used, and a magnetic field is swept perpendicular to the crystallographic a-b plane from -7 T to 7 T. Second-harmonic resistances for (b) detector 1 and (c) detector 2 are shown. A current of 100 μA is applied at the heater strip generating a temperature gradient in $MnPS_3$. The measurements are performed at 8 K, and the separations between the heater and the strips are 1 and 2 μm. The structure in the data between -1 and 1 T is due to an artifact from subtracting the ANE contribution from the data. For more details on subtracting the ANE contribution, see Appendix B.

II. EXPERIMENTAL DETAILS

The transition metal trichalcogenide crystals were bought commercially from the company HQ Graphene [30]. The crystals were magnetically characterized using a magnetic property measurement system to extract the Néel temperature and the magnetization behavior. Figure 1(b) shows the magnetization measurement for an out-of-plane magnetic field. $MnPS_3$ possesses a uniaxial anisotropy perpendicular to the a-b plane. It is generated due to a competition between a dipolar interaction which prefers the spins to lie perpendicular to the a-b plane and a single-ion anisotropy which prefers the spins to lie in the a-b plane [31,32]. The anisotropy field in the OOP direction due to dipolar interaction is stronger, and therefore, the easy axis is perpendicular to the a-b plane. The spin-flop transition is around 3.7 T, as shown in Fig. 1(b), which shows a trend similar to that in [6]. The magnetic susceptibility shows a sharp decrease below 80 K which is the Neél temperature of $MnPS_3$ (see the Supplemental Material [28]).

The crystals were mechanically exfoliated onto a silicon oxide substrate in a nitrogen atmosphere to prevent any oxidation. Two types of devices were fabricated, one with Py detector strips and one with Pt detector strips. The Py and Pt strips were sputtered on the flakes and were 7 nm thick and 200 nm wide. The center-to-center distance between the injector and detector electrodes varies for the different devices between 0.6 and 5 μm. The detector strips were connected to Ti (5 nm)-Au(50 nm) leads which were evaporated on top (see the Supplemental Material [28]).

In order to generate magnons thermally, a charge current was sent through the Py and Pt heater strips to generate a temperature gradient due to Joule heating in the strip. The thermally generated magnons diffuse in the magnetic material and were detected nonlocally via spin-flip scatting with electrons in Pt or Py, generating a spin accumulation in the Pt or Py detector strip. In Pt a charge current was generated via the ISHE, which converts a spin current into a charge current. In a ferromagnetic heavy metal a charge current was generated via the ISHE and the IASHE [26]. The magnitude and directions of the spin current detected by the IASHE depend on the product $\vec{J}_s \times \vec{M}_{Py}$ for spins polarized in the direction of $\vec{M}_{Py}$. Therefore, a Py detector strip can detect an out-of-plane spin accumulation which is controlled via the magnetization direction of Py [25]. For a detailed overview of the IASHE see Appendix A.

An alternating current I was sourced through the Pt and Py injector. The second-harmonic (2f) responses of the nonlocal voltage V were measured across the Pt and Py detectors via a lock-in amplifier. The nonlocal resistance is defined as $R_{NL}^{2f} = V^{2f}/I^2$ [14].

III. RESULTS AND DISCUSSION

Figure 3 shows R_{NL}^{2f} for magnetic field sweeps with the magnetic field applied out of plane for a device with a Py heater and detector strips at various temperatures. An anomalous Nernst contribution due to a temperature gradient in the x-axis direction in the Py strips is subtracted from the measured signal; see Appendix B for more details. R_{NL}^{2f} shows an increase of the signal with magnetic field with a maximum at the SF field which corresponds to the frequency of magnon mode I′ ω_β reaching zero, as shown in Fig. 2(d). At the SF field an abrupt sign change is observed in the data which

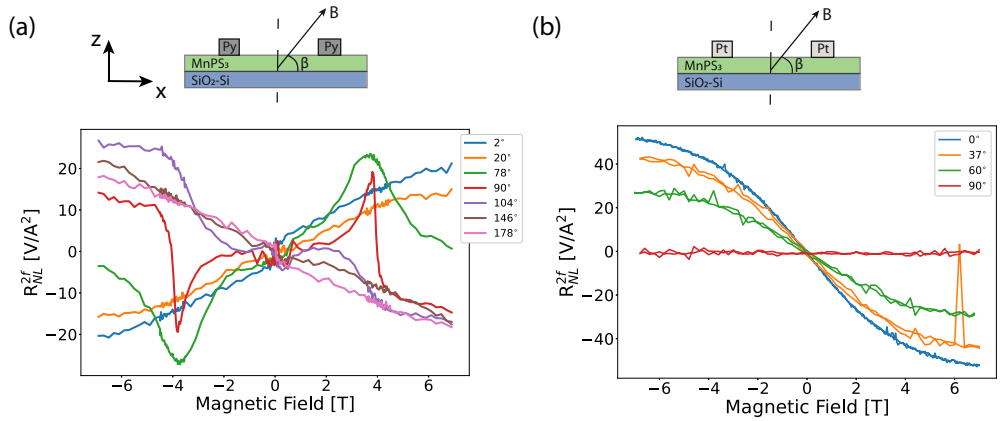

FIG. 4. R^{2f}_{NL} response for (a) Py and (b) Pt heaters and detector strips for a 7T magnetic field applied at various angles of β at 8K. Magnon modes are excited which carry spins polarized in the OOP and/or IP direction depending on the magnetic field direction. The magnons arrive at the detector strips where the Py detectors can detect spins polarized in the IP and OOP direction whereas Pt detectors are only sensitive to IP polarized spins. Detailed overview of the detection mechanism in Py via the IASHE can be found in Appendix A. Comparing Py and Pt detectors, it is clear that at all angles the Pt detector strips do not detect the SF transition. In contrast, the OOP polarized spins are a significant contribution to the spin polarization direction of the magnon modes.

corresponds to the transition of generated magnon modes from Figs. 2(a) and 2(b). This transition results from a sign change of the spin polarization of the magnon modes, similar to the observation in Figs. 3(b) and 3(c).

The directions of the generated charge currents in detectors 1 and 2 are opposite because the directions of the spin currents in detectors 1 and 2 are in opposite directions, as shown in Fig. 3. The charge current generated in the Py strip due to the IASHE depends on $\vec{J}_c \propto \theta_{\mathrm{ASH}}\vec{J}_s \times \vec{M}_{\mathrm{Py}}$. For an OOP applied magnetic field, $\vec{J}_c$ is zero for $\vec{J}_s$ in the z direction and nonzero for $\vec{J}_s$ in the x direction. Therefore, the direction of $\vec{J}_c$ is opposite because the direction of $\vec{J}_s$ in detector 1 is in the $-\hat{x}$ direction and that in detector 2 is in the $\hat{x}$ direction. For more details, see Appendix A.

The applied magnetic field direction determines which magnon modes are excited in the AFM, for example for an IP magnetic field magnon mode III' is excited and for an OOP magnetic field I' is excited. Therefore, the polarization direction of the spins carried by the magnon modes changes when changing the direction of the applied magnetic field. Next to that, the IASHE can detect an IP and OOP polarization of the spin current in Py depending on the orientation β of $\vec{M}_{\mathrm{Py}}$ and the direction of the spin current in Py. Therefore the R^{2f}_{NL} response for various directions of the applied magnetic field, as shown in Fig. 4, is a combination of the detection spins polarized in te IP and OOP direction. For $\beta = 0^\circ$ the detected spin polarization direction is purely IP (x direction) and for $\beta = 90^\circ$ purely OOP (z direction).

A device consisting of Pt heater and detectors is only sensitive to an IP spin polarization direction because it only possesses the ISHE. Therefore R^{2f}_{NL} is maximum for $\beta = 0^\circ$, as shown in Fig. 4(b). Spins with an OOP spin polarization direction are not detected and therefore the SF transition is not detected via the Pt detector strips. Comparing the result of Figs. 4(a) and 4(b) show that at angles between $\beta = 0^\circ - 90^\circ$ magnons with a OOP spin polarization are a significant contribution of the generated magnons due to the SSE and that

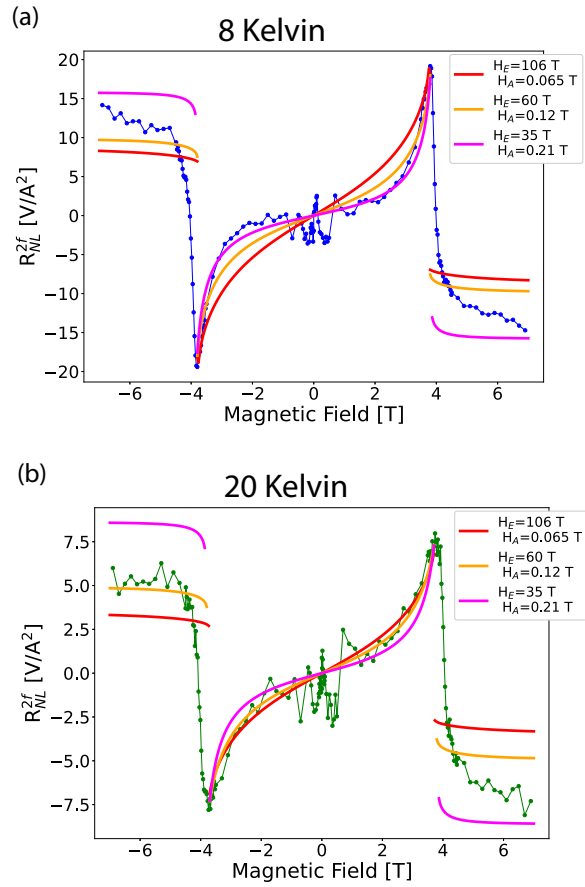

FIG. 5. Measurement shown in Fig. 3(b) for 8 and 20 K fitted for magnetic field values below the SF for various values of H_E and H_A, where $H_E = 106$ T and $H_A = 0.065$ T are the values reported in the literature [31]. We have used $g^{\uparrow\downarrow}_{\mathrm{BSF}}/g^{\uparrow\downarrow}_{\mathrm{ASF}} = 10$ to calculate the response after the SF in order to have the correct order of magnitude. The ratio $g^{\uparrow\downarrow}_{\mathrm{BSF}}/g^{\uparrow\downarrow}_{\mathrm{ASF}}$ is opposite to the ratio found for local measurements on Cr_2O_3-Pt [22], where $g^{\uparrow\downarrow}_{\mathrm{ASF}}$ needs to be larger in order to fit the data. Next to that, the values for C vary between the different fits; for more details see the Supplemental Material, Sec. S11 [28].

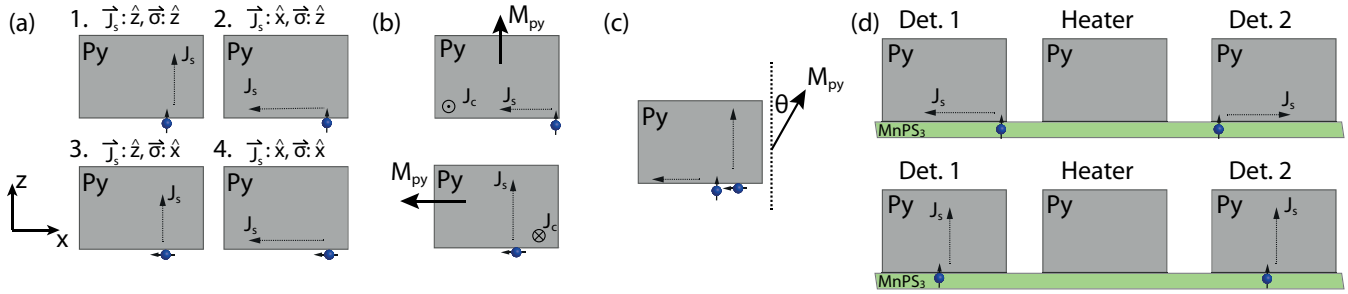

FIG. 6. (a) Possible directions of $\vec{J}_s$ and $\vec{\sigma}$. (b) Situation when $\vec{M}_{\mathrm{Py}}$ is completely out of plane or in plane, which reduces the detection possibilities in (a) to two. (c) Definition of the angle θ. (d) Illustration of possible spin current directions $\vec{J}_s$ for the detectors to the right or left of the heater. $\vec{J}_s$ in the $\hat{x}$ direction results in an opposite contribution to the detected voltage, and $\vec{J}_s$ in the $\hat{z}$ direction results in the same contribution to the detected voltage. Note that we apply large magnetic fields; therefore, we assume that $\vec{M}_{\mathrm{Py}}$ follows the direction of the applied magnetic field.

the IP polarized spins carried by the magnons seems to be completely insensitive to the SF transition.

Xing *et al.* measured Pt-$MnPS_3$ devices for only an in-plane applied magnetic field, whereas we looked at an out-of-plane applied magnetic field and therefore measured the response across the spin-flop transition in $MnPS_3$ [1]. Xing *et al.* measured, for devices consisting of a Pt heater and detectors, a response similar to that in our work for an in-plane applied magnetic field. Next to that, we also do not observe any first-harmonic nonlocal response corresponding to electrically injected and detected magnons (see the Supplemental Material [28]).

The expected signals due to the SSE before and after the spin-flop transition, $\mathrm{SSE}_{\mathrm{OOP\text{-}BSF}}$ and $\mathrm{SSE}_{\mathrm{OOP\text{-}ASF}}$, can be calculated using Eq. (2), and the calculation of S is presented in the Supplemental Material [28] (see also Refs. [33–35] therein). The expected signal due to the SSE is plotted as solid lines in Fig. 5. The magnitude of the expected signal depends on the factor G, Eq. (2), whereas the shape of the expected signal is due to the values of H_{E} and H_A. The calculated second-harmonic response is plotted for various values of H_{E} and H_A, where the ratio of every combination of H_{E} and H_A is kept such that the spin-flop field H_{SF} is the same. Figure 5 suggests that at 8 K H_A is increased and H_{E} is reduced, whereas at 20 K the values of H_A and H_{E} are comparable to the literature values [28,31].

Possible explanations for the change in values of H_A and H_{E} at lower temperatures could be that the single-ion contribution to the anisotropy is reduced and therefore increases the anisotropy strength in the OOP direction due to the dipolar interaction. On the other hand, this would not explain why the exchange interaction strength would decrease. Another explanation could be that the magnon relaxation rate is temperature and magnetic field strength dependent, both of which are kept constant in this calculation. This should be evaluated by an extensive analysis of the temperature and field dependence of the relaxation rate, which is beyond the scope of this paper.

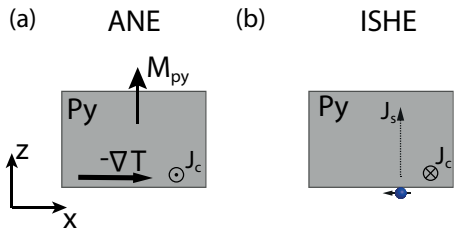

FIG. 7. (a) Anomalous Nernst effect (ANE) and (b) inverse spin Hall effect (ISHE).

IV. CONCLUSION

In conclusion we detected the spin-flop transition in $MnPS_3$ using nonlocal magnon transport to generate the magnons thermally and detect them via the inverse anomalous spin Hall effect using Py detector strips. The measurements were compared to nonlocal magnon transport using Pt detector strips, which are not capable of detecting an out-of-plane spin accumulation, showing the unique power of the IASHE. We found that the magnons change sign when crossing the spin-flop transition, as expected from the magnon modes generated across the SF transition. Next to that, we observed a change in the exchange and anisotropy fields of $MnPS_3$, reaching temperatures below 10 K when we compare the experimental results to the calculated SSE coefficient.

ACKNOWLEDGMENTS

We want to thank Dr. G. R. Hoogeboom and Dr. J. Peiro for the useful scientific discussions and feedback on the interpretation of the data. We acknowledge the technical support from J. G. Holstein, H. Adema T. Schouten, and H. de Vries. We acknowledge the financial support of the Zernike Institute for Advanced Materials and the European Union's Horizon 2020 research and innovation program under Grant Agreements No. 785219 and No. 881603 (Graphene Flagship Core 2 and 3). This project is also financed by the 2016 NWO Spinoza prize awarded to B.J.v.W.

APPENDIX A: ANE, ISHE, AND IASHE IN PERMALLOY

An overview of the various temperature and spin dependent effects in Py is given in this Appendix.

TABLE I. The symmetry relations of the IASHE detection, spin Seebeck effect generation, and the detected voltage due to $\vec{J}_c$ with respect to combinations of (sign-reversed) magnetization, sign reversal of θ, and the detector strip position with respect to the heater.

		IASHE detection			Spin Seebeck generated magnon spin accumulation		Detected voltage due to $\vec{J}_c$		
$\vec{J}_s$	$\vec{\sigma}$	Sign of θ	Sign of $\vec{M}_{\mathrm{Py}}$	Detector position	Sign of θ	Sign of applied magnetic field/$\vec{M}_{\mathrm{Py}}$	Sign of θ	Sign of applied magnetic field/$\vec{M}_{\mathrm{Py}}$	Detector position
$\hat{z}$	$\hat{z}$	odd	even	even	even	odd	odd	odd	even
$\hat{x}$	$\hat{z}$	even	even	odd	even	odd	even	odd	odd
$\hat{z}$	$\hat{x}$	even	even	even	odd	odd	odd	odd	even
$\hat{x}$	$\hat{x}$	odd	even	odd	odd	odd	even	odd	odd

a. Anomalous Nernst effect

The anomalous Nernst effect (ANE) generates a charge current, resulting in a voltage in the detector, under the influence of a temperature gradient perpendicular to the Py magnetization, i.e., $\vec{J}_c \propto \vec{\nabla} T \times \vec{M}_{\mathrm{Py}}$, as shown in Fig. 7(a).

b. Inverse spin Hall effect

The inverse spin Hall effect (ISHE) in Py generates a charge current, resulting in a voltage in the detector, from an injected spin current. The ISHE is independent of the permalloy magnetization direction given by $\vec{J}_c \propto \theta_{\mathrm{SH}} \vec{\sigma} \times \vec{J}_s$ where $\vec{\sigma}$ is the spin polarization direction, $\vec{J}_s$ is the direction of the spin

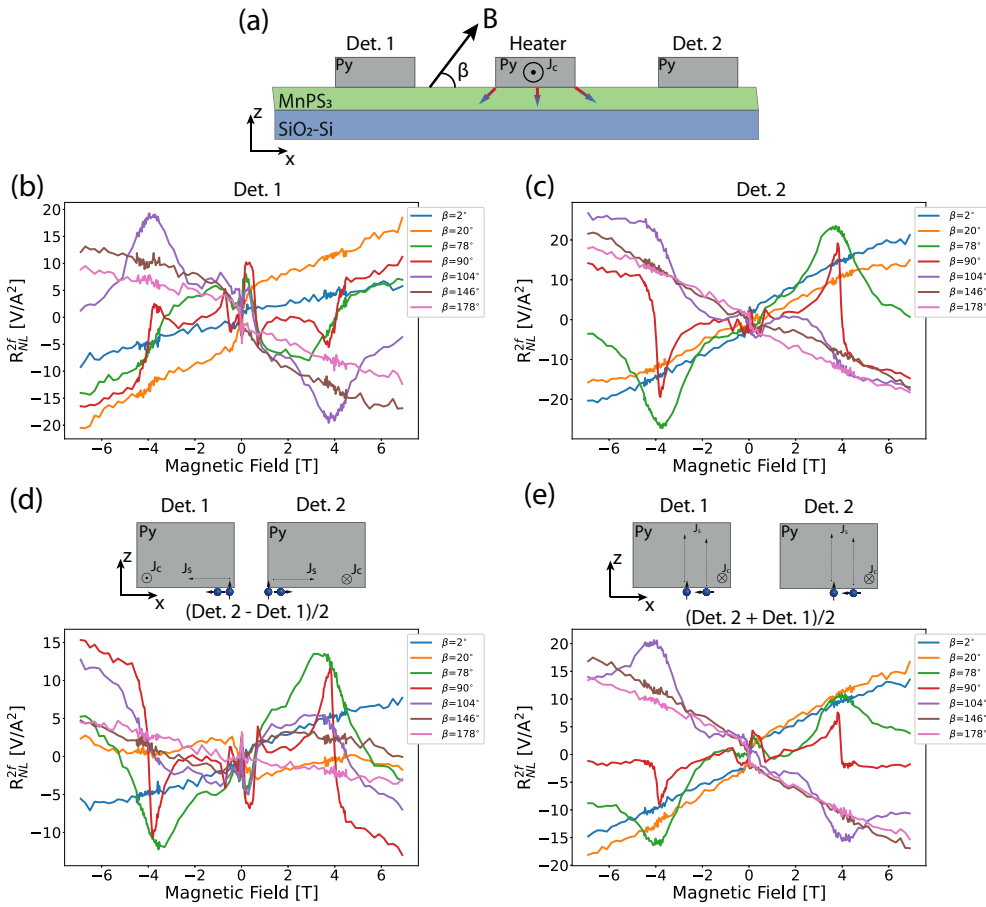

FIG. 8. (a) Illustration of the measurement geometry. The nonlocal second-harmonic response of device 1 is measured at 8 K at various out-of-plane orientations of the applied magnetic field. (b) and (c) The SSE response of detectors 1 and 2, respectively, from which the ANE contribution has been subtracted. The differences and the sum of the responses of detector 1 and detector 2 are shown in (d) and (e), respectively. (d) Detection of the spin current in the $\hat{x}$ direction and (e) detection of the spin current in the $\hat{z}$ direction. We believe that the finite signal at 90° in (e) is due to a slight misalignment of the magnetic field.

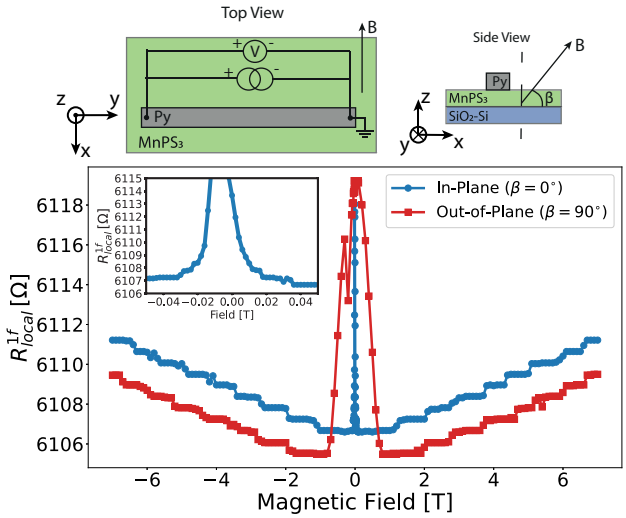

FIG. 9. Anisotropic magnetoresistance measurement of the Py strip to determine the magnetization direction of the Py strip. The magnetic field is applied at angles of $\beta = 0^\circ$ and 90°, and the measurements are performed at 5 K. The steps in the resistances above 1 T are due to signal discretization of the lock-in amplifier.

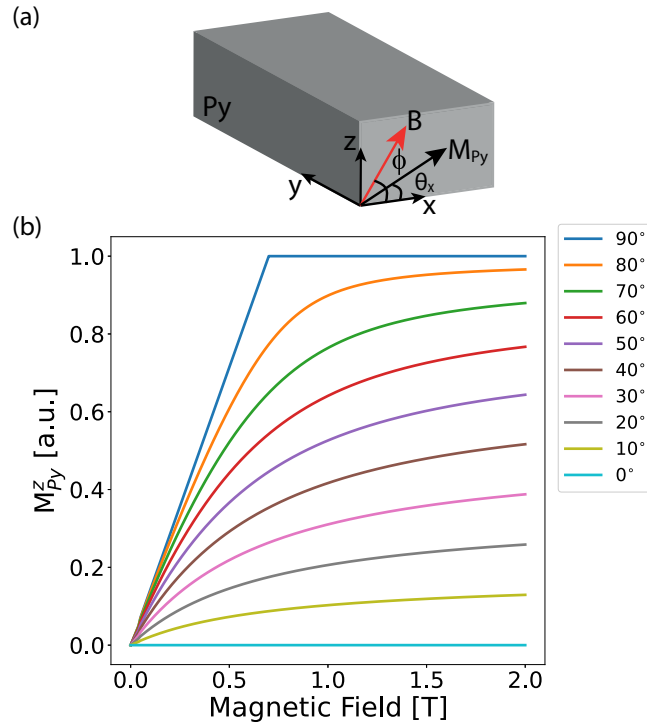

FIG. 10. M^z_{Py} at various angles ϕ using $M^s_{\mathrm{Py}} = 1 \times 10^5$ A/m, $K^y_{\mathrm{Py}} = 0$, $K^x_{\mathrm{Py}} = -5\,\mathrm{kJ/m^3}$, and $K^z_{\mathrm{Py}} = -40\,\mathrm{kJ/m^3}$.

current and θ_{SH} is the spin Hall angle which determines the sign and magnitude of the created charge current for a specific material. The ISHE is illustrated in Fig. 7(b). The ISHE can only detect IP polarized spins and therefore we focus on the IASHE [25,26].

c. Inverse anomalous Hall effect

The inverse anomalous spin Hall effect (IASHE) depends on the projection of the spin polarization on the direction of the Py magnetization and the direction of the spin current: $\vec{J}_c \propto \theta_{\mathrm{ASH}} \vec{J}_s \times \vec{M}_{\mathrm{Py}}$ [25]. We consider two possible directions of the spin current $\vec{J}_s$ in the $\hat{x}$ or $\hat{z}$ direction. Next to that, the spin polarization $\vec{\sigma}$ of $\vec{J}_s$ can have components in the $\hat{x}$ or $\hat{z}$ direction. An overview of the four possibilities is presented in Fig. 6(a).

When $\vec{M}_{\mathrm{Py}}$ is in the $\hat{x}$ or $\hat{z}$ direction, only a spin current in one direction can be detected, as shown in Fig. 6(b), which corresponds to situations 2 and 3 in Fig. 6(a). Therefore, for an out-of-plane ($\hat{z}$-axis) magnetization only out-of-plane polarized spins can be detected, and for an in-plane ($\hat{x}$-axis) magnetization only in-plane polarized spins can be detected.

The IASHE can detect, in general, four different combinations of $\vec{J}_s$ and $\vec{\sigma}$. The relevant factors to take into account are the direction (sign) of $\vec{M}_{\mathrm{Py}}$, angle θ [note that $\theta = \beta - 90^\circ$; see Fig. 6(c)], and the position of the detector strip [see Fig. 6(d)]. These four different combinations of $\vec{J}_s$ and $\vec{\sigma}$ give symmetries for the sign of the detection of the voltage generated by the charge current $\vec{J}_c$ with respect to (1) the $\vec{M}_{\mathrm{Py}}$ direction (positive or negative), (2) sign reversal of θ, and (3) the position of the detector strip with respect to the heater (see Table I). The contribution of a spin current $\vec{J}_s$ in the $\hat{x}$ direction changes sign with respect to the detector position relative to the heater position, and the contribution of a spin current $\vec{J}_s$ in the $\hat{z}$ direction does not change sign with respect to the detector position relative to the heater position. This allows us to distinguish between the effect of $\vec{J}_s$ in the $\hat{x}$ and $\hat{z}$ directions by looking at the differences between and the sum of the measured signals of the two detector strips located on either side of the heater. Next to that, the various spin components generated by the spin Seebeck effect S have certain symmetries with respect to the positive or negative applied magnetic field and sign reversal of θ. Therefore, eight different combinations (direction $\vec{J}_s$, direction $\vec{\sigma}$, and position detector strip) are present, and their symmetries are presented in Table I.

The data from Fig. 4(a) in the main text are shown in Fig. 8(c), and the data for the other detector strip are shown in Fig. 8(b). We can distinguish between the effects of the spin current in Py in the $\hat{x}$ direction [Fig. 8(d)] and the $\hat{z}$ direction [Fig. 8(e)] by calculating the differences and the sum of the measured signals in the two detector strips. $\vec{J}_c$ for the $\beta = 78^\circ$ and $\beta = 104^\circ$ measurements should be the same for a spin current in the $\hat{x}$ direction and opposite for a spin current in the $\hat{z}$ direction, which is indeed observed, as shown in Figs. 8(d) and 8(e). Similarly, by a change from a positive to a negative magnetic field the signal in $\vec{J}_c$ should be reversed, which is true for all measurements. We cannot distinguish between the detected spin polarization direction $\vec{\sigma}$ in the $\hat{x}$ and $\hat{z}$ directions at angles between $\beta = 0^\circ$ and 90° using only the Py strips. This should be compared to the measurements using only Pt strips, which are sensitive to only spins polarized in the $\hat{x}$ (IP) direction, as shown in the main text in Fig. 4.

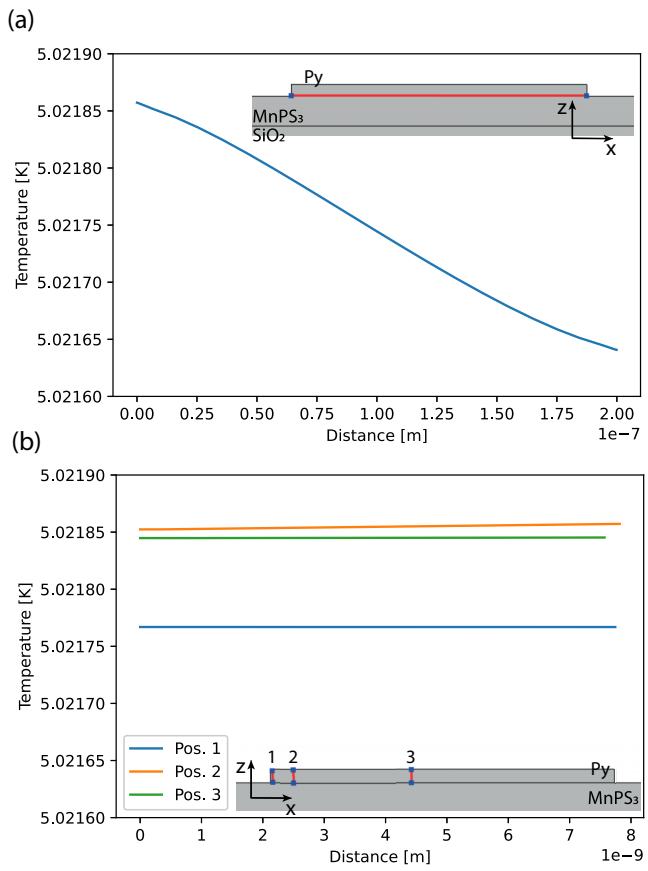

FIG. 11. Temperatures in the Py detector strip along the specific defined lines along the (a) x axis (in plane) and (b) z axis (out of plane), as shown in the insets. The temperature gradient in the Py strip in the z direction is negligible compared to the temperature gradient in the x direction. The base temperature is 5 K, and the injector current is 100 μA at an injector strip separated 2 μm center to center. The parameters used and the procedure to calculate the temperature profile are explained in Sec. S8 of the Supplemental Material.

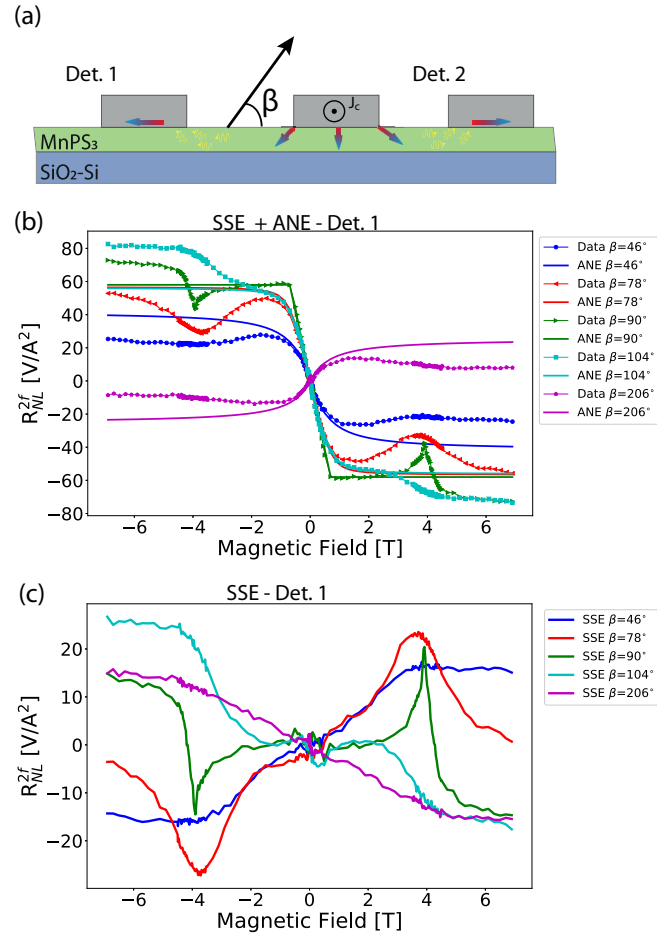

FIG. 12. (a) Illustration of the device geometry, including the directions of the temperature gradients in detectors 1 and 2. (b) The second-harmonic response and the calculated ANE contribution of detector 1. (c) Extracted second-harmonic response in detector 1 due to magnons created by the SSE in $MnPS_3$ at various angles of the applied magnetic field. No background signal is present anymore after the ANE contribution is subtracted.

APPENDIX B: ORIENTATION OF THE PERMALLOY MAGNETIZATION

A change in the magnetization direction in Py changes its resistance due to the anisotropic magnetoresistance, which allows us to deduce the direction of the Py magnetization under the influence of an applied magnetic field in a certain direction by measuring the resistance of the Py strip. A higher resistance is measured when the magnetization is parallel to the current direction, and a low resistance is observed when the magnetization is perpendicular to the current direction. Figure 9 shows the resistance of the Py strip when sweeping an in-plane and out-of-plane magnetic field. The Py magnetization is saturated in the x (z) direction for an in-plane (out-of-plane) applied magnetic field when the resistance is the lowest.

As shown in the inset in Fig. 9, a magnetic field of 40 mT is needed to align the magnetization of Py perpendicular to the strip when a magnetic field is applied along the x direction. Due to magnetic shape anisotropy, an out-of-plane magnetic field along the z direction of 800 mT is needed to orient the magnetization of Py out of plane, perpendicular to the current direction. At higher magnetic fields, the resistances increase due to the ordinary magnetoresistance in the Py strip. Note that there is a small offset around zero applied magnetic field which is due to a small hysteresis in the superconducting magnet.

1. Py magnetization orientation

The magnetization orientation in Py under the influence of a magnetic field is modeled using the same procedure as in the supplementary materials of Ref. [25]. A magnetic field applied in the xz plane is given by $\vec{B} = (B^x, 0, B^z) = (B\cos\phi, 0, B\sin\phi)$, as shown in Fig. 10(a). The magnetic energy density is then given by

$$\varepsilon_{\mathrm{Py}}^{\mathrm{m}} = E_{\mathrm{Py}}^{\mathrm{Zeeman}} + E_{\mathrm{Py}}^{\mathrm{Ani}}, \tag{B1}$$

where $E_{\mathrm{Py}}^{\mathrm{Zeeman}} = -\vec{M}_{\mathrm{Py}} \cdot \vec{B}$ and $E_{\mathrm{Py}}^{\mathrm{Ani}} = \sum_{i=x,y,z} K_{\mathrm{Py}}^{i} \sin^2\theta_i$. The magnetization of Py is defined as $\vec{M}_{\mathrm{Py}} =$

$(M^x_{Py}, M^y_{Py}, M^z_{Py})$, and the angle θ_i is defined as $\cos\theta_i = \frac{M^i_{Py}}{M^s_{Py}}$, where M^s_{Py} is the saturation magnetization of Py.

To determine the orientation of the Py magnetization, we find the minimum energy of $\partial\varepsilon^m_{Py}/\partial\theta_i = 0$ and $\partial^2\varepsilon^m_{Py}/\partial^2\theta_i > 0$. We obtain

$$\cos\theta_x = \frac{M_{Py}B^x}{2\left(K^y_{Py} - K^x_{Py}\right)}, \tag{B2}$$

$$\cos\theta_z = \frac{M_{Py}B^z}{2\left(K^y_{Py} - K^z_{Py}\right)}, \tag{B3}$$

$$\cos^2\theta_y = 1 - \cos^2\theta_x - \cos^2\theta_z. \tag{B4}$$

When a magnetic field is applied in the xz plane, this is valid for an increasing magnetic field until $\cos^2\theta_y = 0$ at B_c, i.e., when $M^y_{Py} = 0$. Above B_c the magnetization lies in the xz plane, and following the same procedure, we find for $B > B_c$

$$M^s_{Py}B^x\sin\theta_x - M^s_{Py}B^z\cos\theta_x = 2\left(K^z_{Py} - K^x_{Py}\right)\sin\theta_x\cos\theta_x. \tag{B5}$$

Combining Eqs. (B2)–(B5), we can model the complete behavior of M^z_{Py} at various angles ϕ of the applied magnetic field. The results for M^z_{Py} are shown in Fig. 10.

2. Subtraction ANE from R^{2f}_{NL}

Due to a temperature gradient in the Py strip a charge current is generated due to the anomalous Nernst effect $\vec{J}_c \propto \vec{\nabla}T \times \vec{M}_{Py}$. Finite-element modeling is used to calculate the temperature gradient in the Py strip [28]. The temperature gradient in the Py strip is predominantly along the x axis and negligible along the z axis, as shown in Fig. 11. Therefore, the ANE generates only a charge current proportional to $\vec{\nabla}_x T \times M^z_{Py}$.

The contribution of the ANE has been subtracted from the second-harmonic response to extract the contribution purely from the SSE. The ANE depends on the magnitude of M^z_{Py} and the temperature gradient along the x axis in the Py strip. The magnitude of M^z_{Py} for a specific field strength and direction is calculated as explained in Sec. B 1. Figure 12(a) shows the measurement geometry and the direction of the temperature gradients in the Py strips of detectors 1 and 2.

Figure 12(b) shows the measured second-harmonic response in detector strip 1 together with the ANE contribution. The ANE contribution in Fig. 12(b) is the magnitude of M^z_{Py} multiplied by a conversion factor which is specific for every detector strip; for detector 1 this is 58 V/A^2. This conversion factor is extracted by fitting the second-harmonic response for $\beta = 90^\circ$ for a magnetic field strength between -1 and 1 T. The ANE contribution for the measurements at all other angles is the M^z_{Py} for the specific angle and magnetic field multiplied by the conversion factor. After subtracting the ANE contribution, the contribution of magnons created via the SSE to the second-harmonic response is the only remaining signal, as shown in Fig. 12(c).

[1] W. Xing, L. Qiu, X. Wang, Y. Yao, Y. Ma, R. Cai, S. Jia, X. C. Xie, and W. Han, Phys. Rev. X **9**, 011026 (2019).

[2] T. Liu, J. Peiro, D. K. de Wal, J. C. Leutenantsmeyer, M. H. D. Guimarães, and B. J. van Wees, Phys. Rev. B **101**, 205407 (2020).

[3] A. Bedoya-Pinto, J.-R. Ji, A. K. Pandeya, P. Gargiani, M. Valvidares, P. Sessi, J. M. Taylor, F. Radu, K. Chang, and S. S. P. Parkin, Science **374**, 616 (2021).

[4] T. Jungwirth, J. Sinova, A. Manchon, X. Marti, J. Wunderlich, and C. Felser, Nat. Phys. **14**, 200 (2018).

[5] V. Baltz, A. Manchon, M. Tsoi, T. Moriyama, T. Ono, and Y. Tserkovnyak, Rev. Mod. Phys. **90**, 015005 (2018).

[6] R. Basnet, A. Wegner, K. Pandey, S. Storment, and J. Hu, Phys. Rev. Mater. **5**, 064413 (2021).

[7] M. V. Costache, M. Sladkov, S. M. Watts, C. H. van der Wal, and B. J. van Wees, Phys. Rev. Lett. **97**, 216603 (2006).

[8] Y. Kajiwara, K. Harii, S. Takahashi, J. Ohe, K. Uchida, M. Mizuguchi, H. Umezawa, H. Kawai, K. Ando, K. Takanashi, S. Maekawa, and E. Saitoh, Nature (London) **464**, 262 (2010).

[9] A. V. Chumak, A. A. Serga, M. B. Jungfleisch, R. Neb, D. A. Bozhko, V. S. Tiberkevich, and B. Hillebrands, Appl. Phys. Lett. **100**, 082405 (2012).

[10] P. Vaidya, S. A. Morley, J. van Tol, Y. Liu, R. Cheng, A. Brataas, D. Lederman, and E. del Barco, Science **368**, 160 (2020).

[11] K. Uchida, S. Takahashi, K. Harii, J. Ieda, W. Koshibae, K. Ando, S. Maekawa, and E. Saitoh, Nature (London) **455**, 778 (2008).

[12] K. Uchida, J. Xiao, H. Adachi, J. Ohe, S. Takahashi, J. Ieda, T. Ota, Y. Kajiwara, H. Umezawa, H. Kawai, G. E. W. Bauer, S. Maekawa, and E. Saitoh, Nat. Mater. **9**, 894 (2010).

[13] S. M. Wu, W. Zhang, A. KC, P. Borisov, J. E. Pearson, J. S. Jiang, D. Lederman, A. Hoffmann, and A. Bhattacharya, Phys. Rev. Lett. **116**, 097204 (2016).

[14] L. J. Cornelissen, J. Liu, R. A. Duine, J. B. Youssef, and B. J. van Wees, Nat. Phys. **11**, 1022 (2015).

[15] S. T. B. Goennenwein, R. Schlitz, M. Pernpeintner, K. Ganzhorn, M. Althammer, R. Gross, and H. Huebl, Appl. Phys. Lett. **107**, 172405 (2015).

[16] J. Shan, L. J. Cornelissen, N. Vlietstra, J. Ben Youssef, T. Kuschel, R. A. Duine, and B. J. van Wees, Phys. Rev. B **94**, 174437 (2016).

[17] R. Lebrun, A. Ross, S. A. Bender, A. Qaiumzadeh, L. Baldrati, J. Cramer, A. Brataas, R. A. Duine, and M. Kläui, Nature (London) **561**, 222 (2018).

[18] G. R. Hoogeboom and B. J. van Wees, Phys. Rev. B **102**, 214415 (2020).

[19] W. Yuan, Q. Zhu, T. Su, Y. Yao, W. Xing, Y. Chen, Y. Ma, X. Lin, J. Shi, R. Shindou, X. C. Xie, and W. Han, Sci. Adv. **4**, eaat1098 (2018).

[20] T. Wimmer, A. Kamra, J. Gückelhorn, M. Opel, S. Geprägs, R. Gross, H. Huebl, and M. Althammer, Phys. Rev. Lett. **125**, 247204 (2020).

[21] J. Li, C. B. Wilson, R. Cheng, M. Lohmann, M. Kavand, W. Yuan, M. Aldosary, N. Agladze, P. Wei, M. S. Sherwin, and J. Shi, Nature (London) **578**, 70 (2020).

[22] D. Reitz, J. Li, W. Yuan, J. Shi, and Y. Tserkovnyak, Phys. Rev. B **102**, 020408(R) (2020).

[23] R. Rodriguez, S. Regmi, H. Zhang, W. Yuan, P. Makushko, E. A. Montoya, I. Veremchuk, R. Hübner, D. Makarov, J. Shi, R. Cheng, and I. Barsukov, Phys. Rev. Res. **4**, 033139 (2022).

[24] R. Wu, A. Ross, S. Ding, Y. Peng, F. He, Y. Ren, R. Lebrun, Y. Wu, Z. Wang, J. Yang, A. Brataas, and M. Kläui, Phys. Rev. Appl. **17**, 064038 (2022).

[25] K. S. Das, J. Liu, B. J. van Wees, and I. J. Vera-Marun, Nano Lett. **18**, 5633 (2018).

[26] K. S. Das, W. Y. Schoemaker, B. J. van Wees, and I. J. Vera-Marun, Phys. Rev. B **96**, 220408(R) (2017).

[27] S. M. Rezende, A. Azevedo, and R. L. Rodríguez-Suárez, J. Appl. Phys. **126**, 151101 (2019).

[28] See Supplemental Material at http://link.aps.org/supplemental/10.1103/PhysRevB.106.224409 for more information.Section S1 gives an overview of the devices. Section S2 gives more information on magnetic susceptibility measurement. Sections S6 and S7 give an extensive overview of the first-harmonic nonlocal measurement results and first- and second-harmonic local results. Section S8 gives the calculation of the temperature gradient in $MnPS_3$ and Py. Section S11 gives the calculation of S.

[29] S. M. Rezende, R. L. Rodríguez-Suárez, R. O. Cunha, A. R. Rodrigues, F. L. A. Machado, G. A. Fonseca Guerra, J. C. Lopez Ortiz, and A. Azevedo, Phys. Rev. B **89**, 014416 (2014).

[30] HQ Graphene, http://www.hqgraphene.com/.

[31] K. Okuda, K. Kurosawa, S. Saito, M. Honda, Z. Yu, and M. Date, J. Phys. Soc. Jpn. **55**, 4456 (1986).

[32] A. R. Wildes, H. M. Rønnow, B. Roessli, M. J. Harris, and K. W. Godfrey, Phys. Rev. B **74**, 094422 (2006).

[33] G. Chen, S. Qi, J. Liu, D. Chen, J. Wang, S. Yan, Y. Zhang, S. Cao, M. Lu, S. Tian, K. Chen, P. Yu, Z. Liu, X. C. Xie, J. Xiao, R. Shindou, and J.-H. Chen, Nat. Commun. **12**, 6279 (2021).

[34] S. M. Rezende, R. L. Rodríguez-Suárez, and A. Azevedo, Phys. Rev. B **93**, 014425 (2016).

[35] F. Kargar, E. A. Coleman, S. Ghosh, J. Lee, M. J. Gomez, Y. Liu, A. S. Magana, Z. Barani, A. Mohammadzadeh, B. Debnath, R. B. Wilson, R. K. Lake, and A. A. Balandin, ACS Nano **14**, 2424 (2020).